Research Article Vol. 32, No. 6 / 11 Mar 2024 / Optics Express 9405
Optics EXPRESS

Broadband 2 × 2 multimode-interference coupler on the silicon-nitride platform

XIHENG AI,[1] YANG ZHANG,[1] WEI-LUN HSU,[1] SYLVAIN VEILLEUX,[2] AND MARIO DAGENAIS[1,*]

[1]Department of Electrical and Computer Engineering, University of Maryland, College Park, MD 20770, USA
[2]Department of Astronomy, University of Maryland, College Park, MD 20770, USA
[*]dage@umd.edu

Abstract: In this paper, we present the design, optimization, and implementation of a sub-wavelength grating (SWG) multi-mode interference coupler (MMI) on the silicon nitride photonic integrated circuit (PIC) platform with a significantly enhanced bandwidth compared to the conventional MMI. We extend the SWG MMI theory, previously presented for the silicon-on-insulator platform, to the Si_3N_4/SiO_2 platform. Our approach involves an initial parameter optimization for a non-paired design, followed by a shift to a paired design that offers a smaller footprint and a broader bandwidth. The optimized SWG MMI exhibits a 1 dB bandwidth of 300 nm for both the insertion loss and power imbalance, making it a significant addition to silicon nitride photonics.

1. Introduction

Based on the self-imaging effect [1], multi-mode interferometers (MMIs) can serve as beam splitters, which are fundamental building blocks for Photonic Integrated Circuits. MMIs offer superior performance compared to y-branches and directional couplers due to their well-defined amplitude, phase, and excellent tolerance [2,3] . Consequently, MMIs find applications in Mach-Zehnder interferometers (MZIs) [4], splitters and combiners [5,6], polarization beam splitters [7]. Studies related to size reduction or performance improvement of MMIs have been published [8–11]. Recently, a design including a sub-wavelength grating with a MMI device on SOI has shown great promises [12,13].

Sub-wavelength gratings (SWGs) are grating structures that utilize a grating pitch smaller than the wavelength [14], suppressing the diffraction effect and exhibiting anisotropic characteristics [12]. By engineering the anisotropic refractive index, SWGs have been employed in many applications such as fiber-chip surface and edge couplers [15–17], microphotonic waveguides [18], lenses [19], waveguide crossings [20], multiplexers [17,21,22], phase shifters [23] and optical switches [24]. Using such a meta-material, the bandwidth of the SWG MMI device has significantly expanded on the SOI platform [12,13], which benefits a wide range of applications including wavelength diplexers [25], broadband polarizer beam splitters [26] and dual-mode beam splitters [27]. Bricked SWG structures have also been proposed to ease the fabrication resolution requirement [28,29].

Beside the SOI platform, other CMOS compatible materials such as silicon nitride, aluminum nitride and lithium niobate has attracted much attention. Silicon nitride (Si_3N_4) stands out as a promising candidate due to its ultralow loss [30], nonlinear characteristic [31], transparency from 400 nm to mid-infrared [32]. Like the SOI platform, there is a strong interest in achieving a high performance MMI devices within the silicon nitride platform.

In this paper, we extend the SWG MMI theory from the SOI platform to other integrated photonic platforms, focusing specifically on a 300 nm thick silicon nitride platform. Our objective is to design and optimize a SWG MMI device with a small footprint and wide operational

#513796 https://doi.org/10.1364/OE.513796
Journal © 2024 Received 21 Nov 2023; revised 31 Jan 2024; accepted 9 Feb 2024; published 1 Mar 2024

Optics EXPRESS

bandwidth. Based on the characteristics of the "paired" and "non-paired" MMIs, we propose a two-step strategy: initially optimizing the parameters based on a "non-paired" design that has more fabrication tolerance and subsequently transitioning to a "paired" design with smaller size. To the best of our knowledge, it is the first demonstration of the SWG MMI working under the paired condition.

Also, we investigate an oscillation noise in the SWG MMI device and identify its source. To eliminate potential noise sources, we employ a chirped SWG MMI design to rule out the grating effect then increase the separation between the two coupling waveguides to suppress the directional coupling effect.

We demonstrate a broadband SWG MMI operating under paired condition on the silicon nitride platform. The 1 dB bandwidth for both insertion loss and power imbalance reaches 300 nm, providing a high-performance building block for the silicon nitride photonics platform. These technical advancements pave the way for future applications in astrophotonics, optical switching, programmable photonic circuits, and quantum information.

2. Working principle for conventional and subwavelength MMI coupler

2.1. General interference

Based on the self-imaging principle, the MMI can produce single or multiple images of the input field [3]. Figure 1(a) shows the geometry of a conventional 2×2 MMI. The fundamental mode in one of the input ports excites a series of modes in the multimode section region:

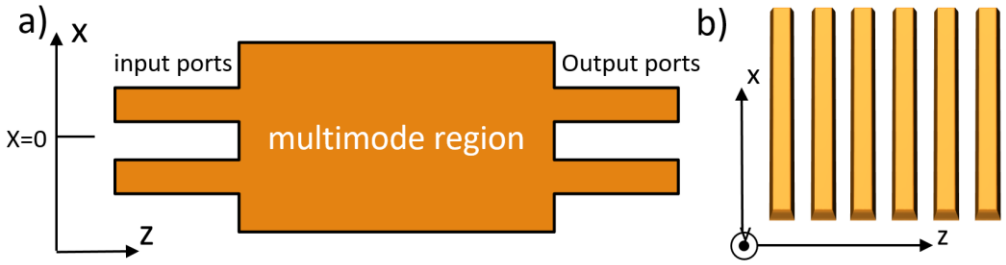

Fig. 1. a) Schematic model of a 2×2 MMI. b) Subwavelength grating structure

$$\varphi_{in}(x) = \sum_m c_m \varphi_m(x), \tag{1}$$

where c_m are the field excitation coefficient and φ_m are the bounded modes in the slab which have propagation constants β_m. As these excited modes propagate in the multimode region, they generate one or several images of the input field at certain distances, determined by the beat length L_π of the two lowest-order modes.

$$L_\pi(\lambda) = \frac{\pi}{\beta_1 - \beta_2}, \tag{2}$$

which can be approximated as

$$L_\pi(\lambda) = \frac{4 n_{core} W_{MMI}^2}{3\lambda}, \tag{3}$$

where W_{MMI} and n_{core} are the effective width and effective refractive index of the multimode region, respectively. The effective width of the MMI may slightly differ from the actual size due to the Goos-Hänchan shift [3]. For the 2×2 MMI that we discuss in this work, if it does not work under the paired condition, the first double image appear at the length of $3L_\pi/2$ as the power propagates in the multimode region (shown in Fig. 2(a)).

Optics EXPRESS

2.2. Paired interference

By launching an even symmetric input field at $x = \pm W_{MMI}/6$ we can excite the modes selectively. In this way, the modes with mode number m = 2,5,8... are not excited and the modes with number 0-1, 3-4, 6-7... contribute to the imaging in pairs. As a result, the period length of self-imaging is reduced by a factor of three and the first double image appears at a length of $L_\pi/2$.

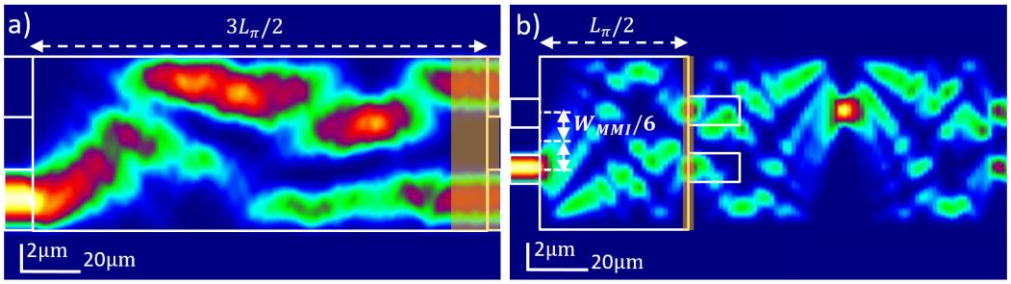

Fig. 2. Simulation results of the conventional a) non-paired and b) paired MMI with the same width. Here we only model the input ports and a long multimode region to show the power distribution. The output ports can be set at the double image positions to collect the light. The yellow regions show the tolerance of each device.

Figure 2 shows the simulated power distribution for the non-paired and the paired conventional MMIs (the simulation software and methods will be discussed in the simulation section). For this simulation, we only model the input ports and a long multimode region to show the power distribution for a longer distance without being stopped by the output ports. We can set the output ports at the double image position to collect the light.

For the non-paired case in Fig. 2(a), there is no restriction for the input position. For the paired condition the input port has to be set at the $\pm W_{MMI}/6$ (see Fig. 2(b)), so the width of the ports should be narrower to avoid coupling between them. While the double image still exists at $3L_\pi/2$, we see a new double image at $L_\pi/2$ in Fig. 2(b). The footprint of the MMI can be reduced if the output ports are set there.

2.3. Subwavelength grating MMI coupler

Due to the bandwidth limitation inherent in the conventional MMI, the subwavelength grating (SWG) structure has been introduced as a solution to enhance the bandwidth. Based on the theory established for SOI platform [12], here we further generalize it to another material. SWG is the grating structure which has a period smaller than one half of the effective wavelength of the light: $\Lambda < \frac{\lambda}{2n_{eff}}$. In that way the grating structure can avoid the Bragg grating limitation and act as an anisotropic material.

Similar to normal anisotropic crystals, the SWG material can be described by refractive index in x, y, and z directions (see Fig. 1(b)). For an anisotropic MMI, the beat length can be approximated as:

$$L_\pi^{SWG}(\lambda) = \frac{4W_{MMI}^2}{3\lambda}\frac{{n_{zz}}^2}{n_{xx}} = \frac{4W_{MMI}^2}{3\lambda}n_{SWG}, \tag{4}$$

where n_{zz} and n_{xx} are the refractive indices in the z and x directions, respectively. When the duty cycle is set to be 50%, the anisotropic refractive indices n_{xx}, n_{zz} can be expressed as [33]:

$$n_{xx} = \left(\frac{{n_{core}}^2+{n_{clad}}^2}{2}\right)^{\frac{1}{2}}, \tag{5}$$

$$n_{zz} = \left(\frac{2}{\frac{1}{{n_{core}}^2}+\frac{1}{{n_{clad}}^2}}\right)^{\frac{1}{2}}, \tag{6}$$

Optics EXPRESS

where n_{core} and n_{clad} represent the effective refractive indices for the core and cladding material. Note here that n_{core} and n_{clad} are the 2D effective refractive indices, which should already include the influence of the vertical boundaries (in the y direction). To calculate this 2D n_{core} with the y direction boundaries, we simulate an infinite large 300 nm thick Si_3N_4 slab, sandwiched by SiO_2 layers. The relationship between n_{core} and the wavelength is shown in Fig. 3(a).

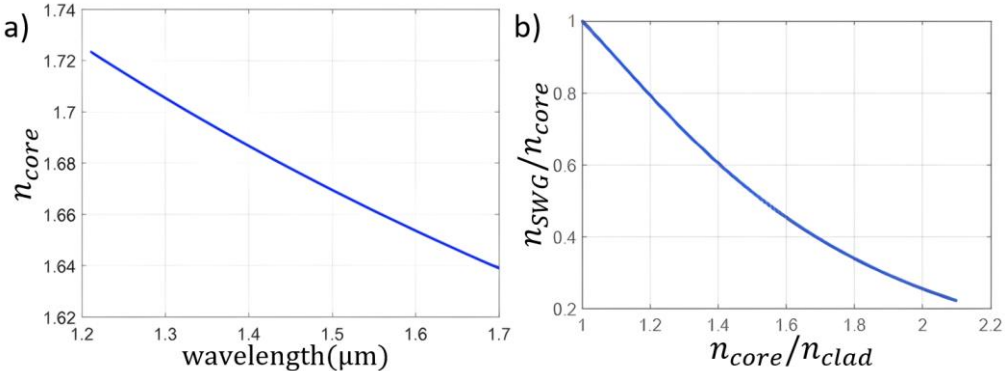

Fig. 3. a) Relationship between n_{core} and the wavelength by simulating a 300 nm thick Si3N4 slab sandwiched by SiO2 cladding.n_{core} decreases as the wavelength increases. b) Relationship between the beat lengths of the SWG MMI and the conventional MMI represented by n_{SWG}/n_{core} and n_{core}/n_{clad} ratio.

In a conventional MMI, the beat length L_π exhibits significant variation with wavelength λ which results in a narrow bandwidth. For the beat length shown in Eq. (3), there are two terms related to the wavelength: $1/\lambda$ and $n_{core}(\lambda)$. Both terms decrease as the wavelength increases, so the beat length deviate from the designed value as the wavelength varies.

After analyzing the limitation of bandwidth for the conventional MMI, now we consider the case for the SWG MMI. $n_{core}(\lambda)$ is now replaced by $n_{SWG} = \frac{n_{zz}^2}{n_{xx}}$ in the beat length expression shown in Eq. (4). According to Eq. (5) and (6), we can rewrite $\frac{n_{zz}^2}{n_{xx}}$ as a function of n_{core} and n_{clad}:

$$n_{SWG} = \frac{n_{zz}^2}{n_{xx}} = \left(\frac{8n_{core}^4 n_{clad}^4}{(n_{core}^2+n_{clad}^2)^3}\right)^{\frac{1}{2}} \tag{7}$$

Now we compare the wavelength dependence between the conventional MMI and the SWG MMI by dividing n_{SWG}byn_{core}. We plot n_{SWG}/n_{core} as a function of $n_{core}(\lambda)/n_{cladding}(\lambda)$, based on Eq. (7) (see Fig. 3(b)). Since $n_{cladding}(\lambda)$ only has the material dispersion which is less than 0.5% from 1200 nm to 1700nm [34], $n_{core}(\lambda)$ plays the major role here. As the wavelength increases, $n_{core}(\lambda)/n_{cladding}(\lambda)$ decreases, and n_{SWG}/n_{core} increases.

Although both $L_\pi^{SWG}(\lambda) = \frac{4W_{MMI}^2}{3\lambda} n_{SWG}$ and $L_\pi(\lambda) = \frac{4W_{MMI}^2}{3\lambda} n_{core}$ suffer from a decrease when λ increases, $L_\pi^{SWG}(\lambda)$ shrinks relatively slower. In conclusion, applying SWG structure to the MMI coupler will decrease the variation of the beat length at different wavelengths, thereby increasing the bandwidth of the device.

3. Design and simulation

3.1. Device design (SWG MMI, taper)

The width of the MMI coupler is a critical design parameter as it needs to be wide enough to support an adequate number of modes. However, a wider MMI width corresponds to a longer device length, leading for a narrower bandwidth. To strike a balance, we have chosen a width of

Optics EXPRESS

12 μm, which can support eight modes and corresponds to an acceptable MMI length for our design. Note that, because of the Goos-Hänchan shift we mentioned above, the effective MMI width W'_{MMI}=12.3 μm is slightly larger than the physical size.

The position and the width of the input/output ports depend if it is a paired or a non-paired design. In the paired design, the separation of the ports needs to be $W'_{MMI}/3$, which imposes limitations on the port width due to the small separation between the ports while the port width of the non-paired design can be larger.

For the paired MMI, the separation between the two ports is $W'_{MMI}/3$ = 4.1 μm. The port width $W_{port(paired)}$ is set to be 2.5 μm to ensure efficient mode excitation in the multimode region while avoiding coupling between the ports, as shown in Fig. 4(a). The width of the waveguides supporting the fundamental TE mode on a 300 nm Si_3N_4 platform is designed as W_{WG}=1μm. Tapers between the ports and the single mode waveguides are utilized to reduce the coupling loss. The grating width tapers from an input width W_{wg} to a final width of $W_{port(paired)}$. The core width tapers down from W_{WG} to 0 to match the effective refractive index in the MMI region. The length of the multimode region and the tapers will be determined through simulation. For convenience in our analysis and fabrication, we set the duty cycle of the grating to be 50%. The period length is set to be Λ=400 nm to avoid the Bragg grating condition.

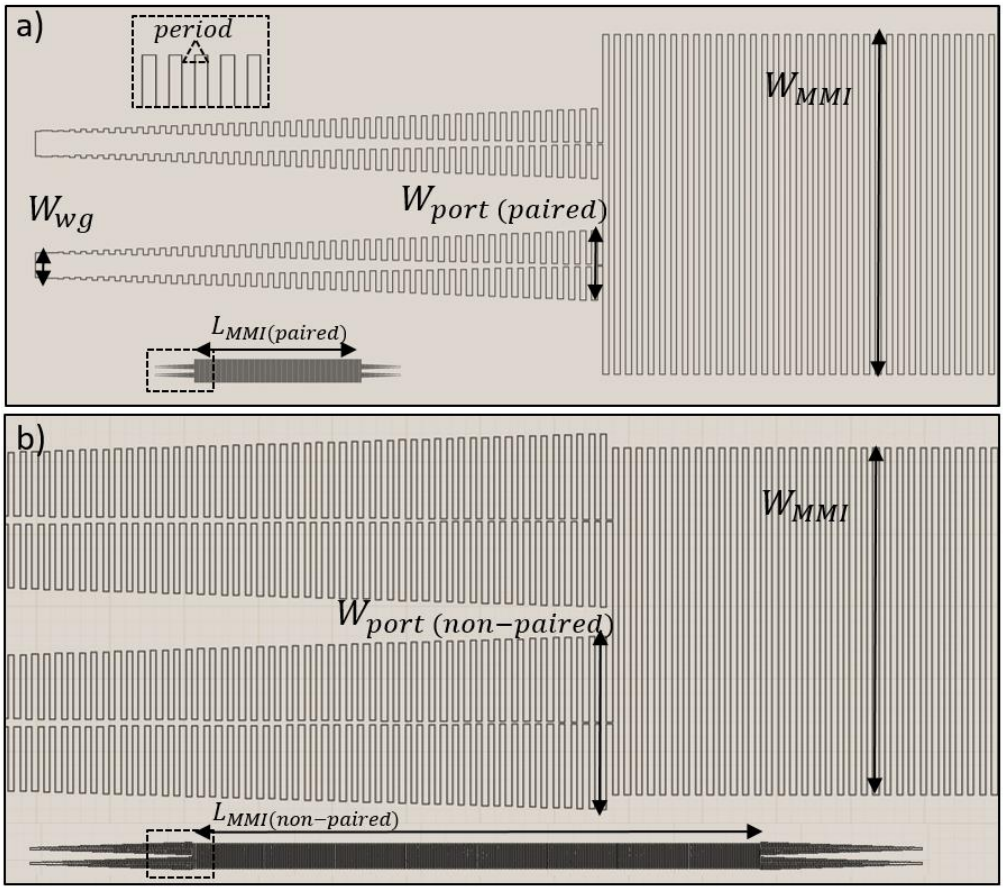

Fig. 4. Layout structures of a) the paired SWG MMI b) the non-paired SWG MMI. The pattern in the black boxes are zoomed to show the grating details. They share a MMI width of W_{MMI}=12μm.

Optics EXPRESS

In the non-paired MMI, we can set the port width as large as possible. The port width is set to be $W_{port(non-paired)}$=5.5μm so that the edge of the ports reaches the edge of the multimode section and a 1μm gap remained between the ports to avoid coupling, as shown in Fig. 4(b).

On the other hand, the actual beating length L_π^{real} may be different from the simulated L_π because of the fabrication errors. Even with a careful control, the deposition rate of the Si_3N_4 layer, the etching quality of the SWG structure and the conformity of the SiO_2 top cladding deposition may not be perfect. However, these errors don't affect the principle of the multimode interference. As long as the device works as an MMI, only the beat length changes because of the fabrication errors. We can do the optimization by sweeping the MMI length experimentally.

An observation helps to make this process easier. From Fig. 2 we notice that the power distribution configuration is more continuous in the non-paired MMI and is more scattered in the paired case (note that, since FIMMwave is not able to provide clear power distribution configuration of a device with too many sections, we use the configuration of the conventional MMIs to show the behavior of paired and non-paired MMIs). When we sweep the MMI length of the non-paired device $L_{MMI(non-paired)}$(see Fig. 4), the output ports can collect the light in a wider range near $3L_\pi/2$ (see the yellow box in Fig. 2(a)). On the other hand, the paired MMI can only be functional when the position of the output ports is accurate. This difference of fabrication tolerance is also mentioned in [35].

Since the paired MMI has a smaller footprint while the non-paired MMI has more fabrication tolerance, we adopt a two-step strategy by optimizing the non-paired and paired SWG MMI devices in sequence (see Fig. 5). While sweeping the length of the MMI region, the non-paired device is more likely to be functional within a relatively wide range around $3L_\pi^{\text{real}}/2$. After obtaining the MMI length $L_{non-paired}^{\text{real}} \approx 3L_\pi^{\text{real}}/2$ from this process, we can get the approximated L_π^{real} which is shared by the paired MMI. As the second step, since the length of the paired MMI should be $L_\pi^{\text{real}}/2$, we sweep the parameters around $L_{non-paired}^{\text{real}}/3$. It is worth noting that the paired MMI length L_{paired}^{real} is not necessarily $L_{non-paired}^{\text{real}}/3$ because L_{paired}^{real} need to be closer

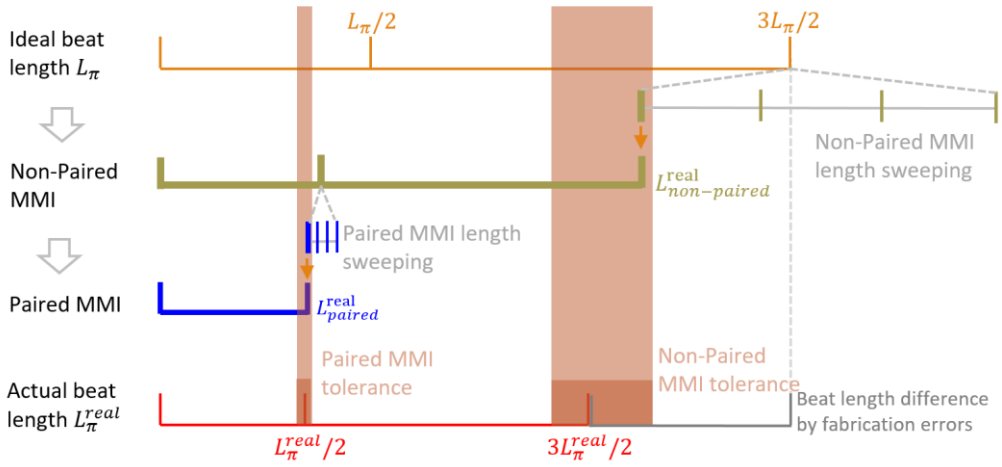

Fig. 5. Work flow of the two-step strategy. The actual beating length L_π^{real} may be different than the simulated value L_π which is calculated under the ideal condition. As we discussed, the tolerance of the non-paired MMI is higher than for the paired MMI. So, we first sweep the length of non-paired MMI to produce a functional device at $L_{non-paired}^{\text{real}}$. Then we sweep the length of the paired MMI around $L_{non-paired}^{\text{real}}/3$ with a smaller step size. After the finer scan we can produce the paired SWG MMI.

Optics EXPRESS

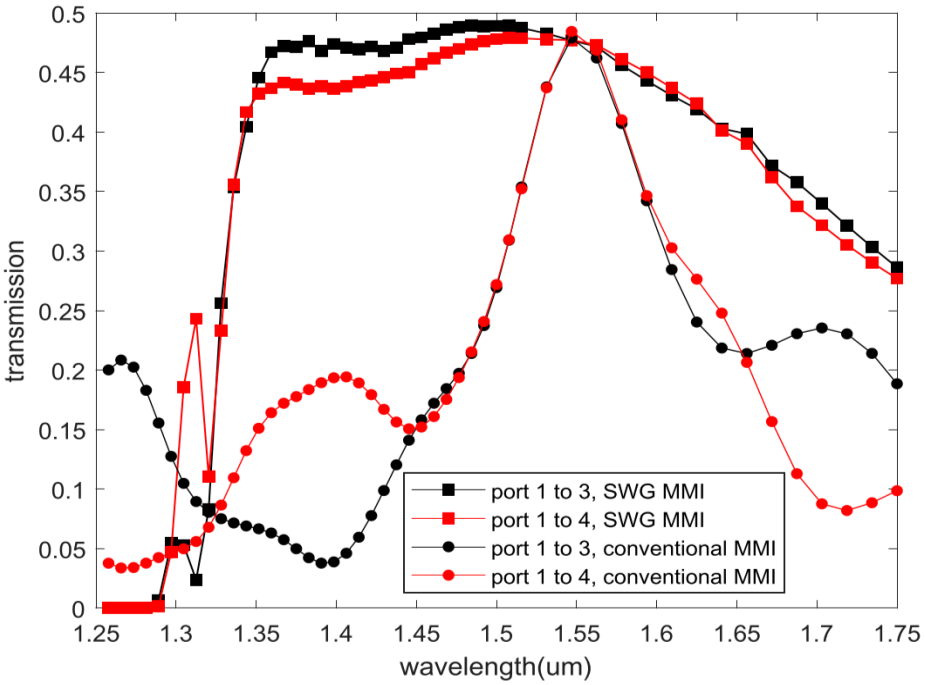

Fig. 6. Simulation transmission spectrum at two output ports of SWG MMI and conventional MMI. Both are designed under paired condition and have the same width of 12μm. Even with the Bragg grating effect around a wavelength of 1.3μm, the SWG MMI shows a larger bandwidth compared with its conventional counterpart (the port numbering is shown in Fig. 7).

to $L_{\pi}^{\text{real}}/2$ while the non-paired MMI can be functional when $L_{non-paired}^{\text{real}}$ is slightly away from $3L_{\pi}^{\text{real}}/2$. After a finer sweep, we can produce a paired SWG MMI with a smaller footprint.

Additionally, since our device is designed for TE modes, a TM filter has been added to reduce the TM noise. This TM filter consists of a set of 90-degree bends with a radius of 50μm. By leveraging the different bending losses of the fundamental TE and TM modes, the TM noise can be effectively suppressed while the TE mode experiences minimal loss (see detailed discussion in our previous work [36]).

3.2. Simulation using Fimmwave

The simulations are performed on the Photon Design FIMMWAVE/FIMMPROP [37], a simulator software based on the Eigenmode expansion method (EIM). Given the complexity of the grating structure, MATLAB scripts are used to establish the model by invoking the built-in FIMMWAVE commands. To save simulation time, we employ the quasi-2D solver and primarily focus on the simulation of the paired MMI. We note that the effective refractive index of a 300 nm thick slab should also be calculated by simulation so that it can be applied to the quasi-2D simulation.

In the EIM solver, a device is divided into sections, with each section considered as a straight waveguide. The solver obtains the mode set in those waveguides and calculates the coupling efficiency between the mode sets as they propagate along the device. Since in the SWG multimode region there are sections filled with cladding material only, there is no bounded mode naturally. To deal with that, we set the mode number to be 200 so that a large number of unbounded modes are taken into account in these “no core section”.

Optics EXPRESS

The optimization is performed at 1550 nm wavelength. While other parameters such as the MMI width, the port positions and the grating period have been determined in section 3.1, we sweep the MMI length and the taper length so that the transmissions from both output ports get as close to 50% as possible.

Based on the simulations, we optimized the paired SWG MMI length L_{MMI}=102μm (corresponding to a beat length L_{π}=204μm) and the taper length L_{taper}=21.2μm. We plot the power coming from both output ports as a function of wavelength (see Fig. 6). The bandwidth is much larger for the SWG MMI than that for the conventional MMI with the same MMI width (W_{MMI}=12μm). It is worth noting that the drop near the wavelength λ=1.35μm is due to the Bragg grating limitation. According to the Bragg reflection equation $\lambda_{Bragg} = 2L_{period}n_{eff}$, if a good performance at shorter wavelengths is desired, we can further decrease the Bragg grating reflection wavelength by choosing a smaller grating period.

4. Fabrication and characterization

4.1. Fabrication and measurement

The silicon nitride layer is deposited using low-pressure chemical vapor deposition (LPCVD) on a silicon substrate wafer with a 5μm thermal oxide layer. A positive resist, ZEP-520A is spin-coated on the top of the sample for e-beam lithography (EBL) purpose. AQUAsave is applied to the resist to prevent the accumulation of electrons during the e-beam writing process. The EBL process uses a 100 kV Elionix ELS G-100 system. To avoid stitching error in the SWG region, the writing field is chosen to be 500μm x500μm, which encompasses the major part of the device. After developing, the pattern is transferred to a 10 nm Chromium hard mask using a lift-off process. The silicon nitride layer is dry etched using an ICP-RIE system (Oxford Plasmalab System 100). Finally, the remaining Chromium mask is removed using a Cr wet etching process, and a 5μm silicon dioxide cladding is deposited through Plasma Enhanced Chemical Vapor Deposition (PECVD). Figure 7 depicts the Scanning Electron Microscope (SEM) images of one of the fabricated devices.

The performance of the SWG MMI is first measured by a TE polarized Keysight 8164B LMS Mainframe/81600B Tunable Laser source with a tuning range of 1450-1640 nm. The high resolution of this source allows us to analyze the spectrum in detail. The light is edge coupled in and out of the chip using polarization maintaining fibers, the position of which can be adjusted by the motorized stages. After matching the fibers and the waveguides, the coupling efficiency is about 3 dB/facet. The output power is measured using the Keysight N7744A optical analyzer (see Fig. 8).

Based on the transmission spectrum we get, we evaluate the MMI performance by measuring the insertion loss: $\mathrm{IL(dB)} = 10\log(I_{port3} + I_{port4})$ and power imbalance $\mathrm{PI(dB)} = 10\log(I_{port3}/I_{port4})$ where I_{port3} and I_{port4} represent the power collected from port 3 and port 4, normalized by the input power at port 1 (see the port numbering in Fig. 7(a)).

4.2. Oscillation and super-mode

Before proceeding forward, an oscillation issue observed in the measured transmission spectrum needs to be dealt with. Figure 9(a) shows the normalized transmission spectrum measured at both ports of a SWG MMI device. Here we observe an oscillation starting from 1550 nm, while the transmission spectrum is supposed to be smoother. Figure 9(b) shows the power imbalance calculated from these transmission lines, where the oscillation is more obvious, reaching an oscillating amplitude of 5 dB around 1640 nm. This oscillation problem makes it impossible to control the insertion loss and power imbalance within a wavelength band.

Since such an oscillating behavior is not observed in the simulation, we believe it is caused by reasons that are not considered by the software. Experimental tests should be performed to

Optics EXPRESS

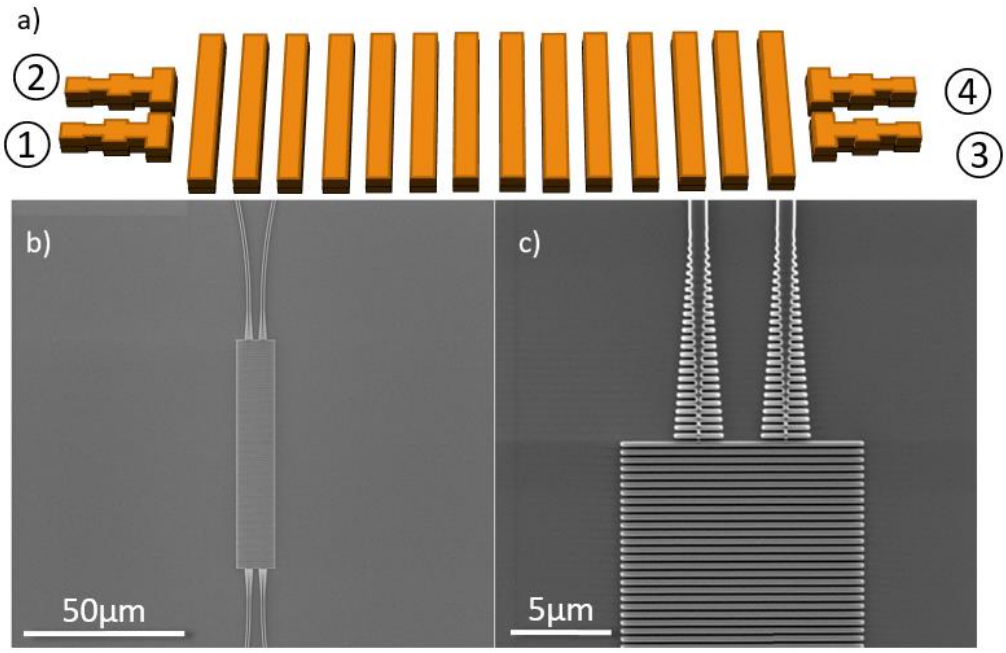

Fig. 7. a) Schematic of a SWG MMI in paired working condition b,c) SEM images of the fabricated SWG MMI, prior to the deposition of the SiO2 top cladding.

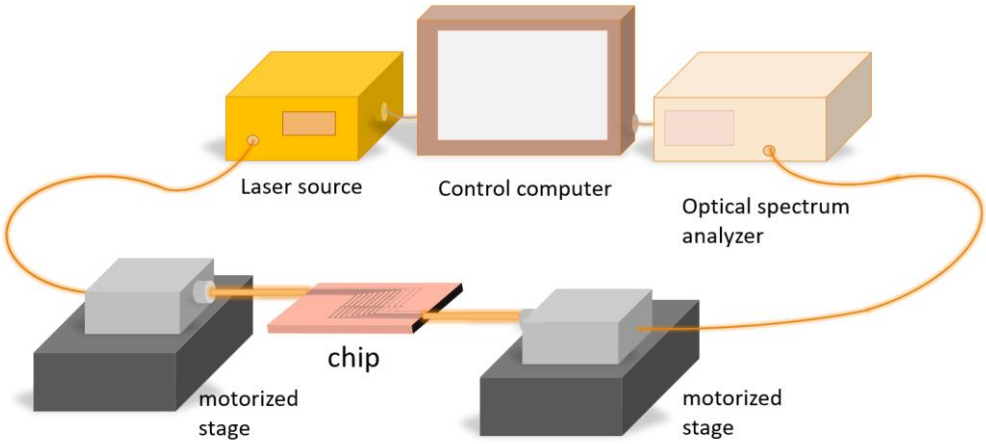

Fig. 8. Schematic experimental setup

analyze the cause. Here we design two experiments to investigate the possible causes: the grating effect in the multimode region and the directional coupling effect in the routing waveguides.

Suspecting that the oscillation is caused by the grating effect in the multimode region, a chirped grating design has been employed. For the SWG structure, the anisotropic characteristic originates from the mixing of core and cladding materials, while the common usages of the gratings such as refracting and reflecting are not utilized. Actually, the period length is designed to be "subwavelength" to avoid these grating effects.

Now assuming the oscillation is a behavior caused by the grating effect, we chirp the grating to further reduce its influence. Here we vary the grating period from Λ=400 nm to Λ=200 nm

Optics EXPRESS

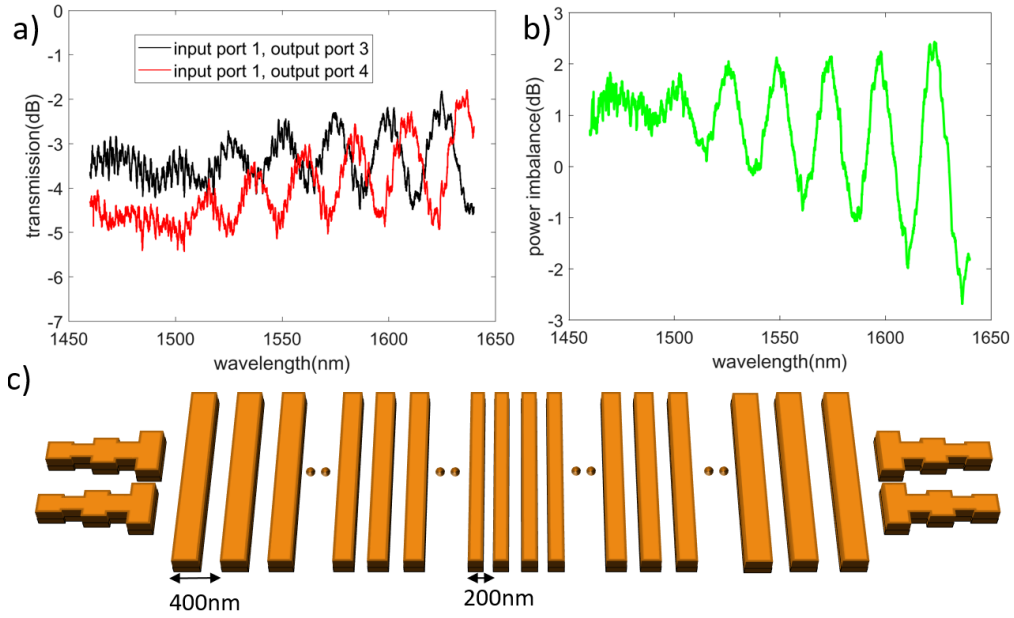

Fig. 9. a) Transmission spectra at the two output ports (ports 3 and 4) of the SWG MMI from experimental measurement. b) Power imbalance of the two output ports. The oscillation becomes more obvious in the power imbalance, reaching approximately 5 dB around 1640 nm. c) Schematic model of the chirped SWG MMI design

and then back to Λ=400 nm (see Fig. 9(c)). In that way, we break the periodicity of the grating, the oscillation should disappear if it is caused by the grating effect. Actually, it is similar to the phenomenon where the side lobe of the Bragg grating spectrum disappears when the grating is chirped linearly [38].

Note that the effective refractive index of the SWG material should remain the same because it relies only on the duty cycle which remains 50%, but not on the period length. The measurement result shows, even with the chirped SWG MMI, the experimental results still exhibited oscillation with a similar amplitude, indicating that the oscillation is not directly related to the SWG structure.

Next, we investigate the directional coupling effect in the waveguides that connect the SWG MMI to the fibers. As shown in Fig. 10, the power is transferred from the output ports of the SWG MMI to the edge of the chip by the routing waveguides, where their widths are tapered down from 1μm to 0.3μm to expand the mode size. The mode mismatch is minimized to reach a high coupling efficiency between these narrow coupling waveguides and the fiber. On the other hand, the power is less bounded in them, making the directional coupling effect more possible.

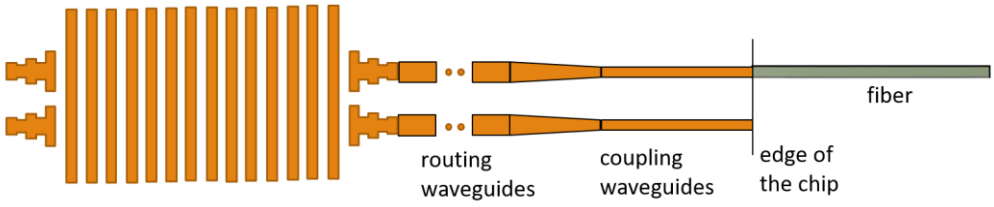

Fig. 10. Schematic diagram of the chip-to-fiber coupling.

Optics EXPRESS

We increase the separation between the coupling waveguides from 30μm to 100μm to reduce the coupling strength. As a result of this test, the oscillation disappears, showing that the cause of this oscillation is due to the directional coupling effect.

4.3. Two-step strategy

As mentioned above, we first fabricate the non-paired device which is more tolerant experimentally. Based on the simulated beat length L_π=204μm, the MMI length $L_{MMI(non-paired)}$ should be around $3L_\pi/2$=306μm. After sweeping the non-paired SWG MMI length with a step size of 10μm, we achieved an optimized MMI length $L_{MMI-nonpair}$= 280μm where the insertion loss is the lowest among the tested devices. The measured insertion loss for the optimized device is presented in Fig. 11. We observe that the total insertion loss remains within 1.5 dB across a wavelength range of 1450-1640 nm.

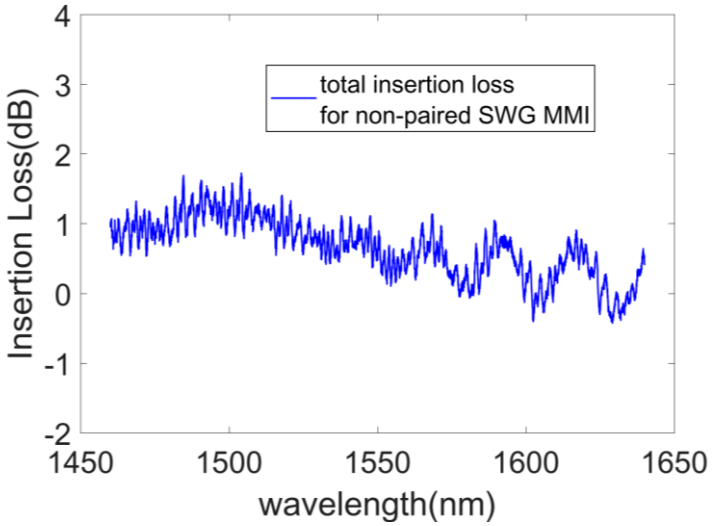

Fig. 11. Measured total insertion loss of the non-paired SWG MMI with a MMI length $L_{MMI-nonpair}$= 280μm. The insertion loss is under 1.5 dB within the measuring range.

As the second step, we fabricate the paired SWG MMI based on the parameters we obtain from the non-paired SWG MMI. The estimated MMI length is around $L^{\text{real}}_{non-paired}/3$ = 93.3μm. We scan the length of MMI by a step size of 2μm to optimize the paired SWG MMI and find the optimized MMI length to be L^{real}_{paired}=90μm.

4.4. Measurement results

A broadband diode laser and an Optical Spectrum Analyzer have been used to measure the spectrum for the paired SWG MMI over a wider spectral range. As shown in Fig. 12, within a 300 nm bandwidth centered around 1550 nm, both the insertion loss and the power imbalance remain below 1 dB. Moreover, within a narrower range spanning over 50 nm near 1450 nm, both the insertion loss and power imbalance were found to be below 0.5 dB.

Optics EXPRESS

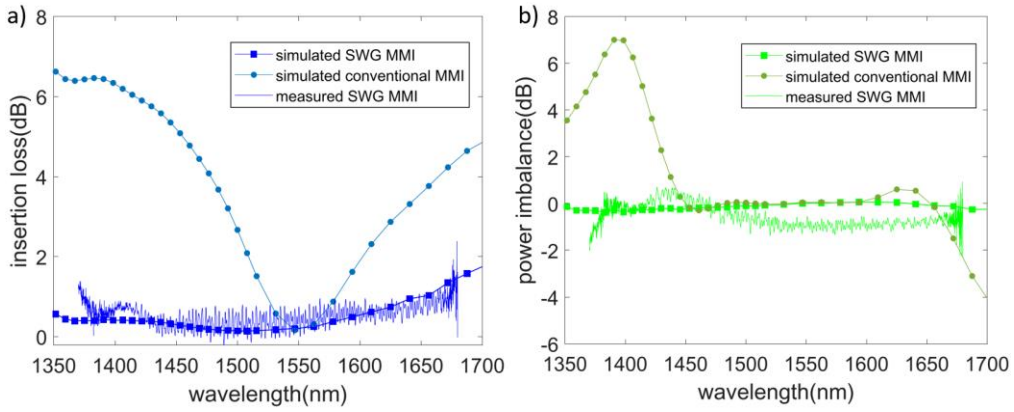

Fig. 12. Measured performance of the paired SWG MMI on Si3N4 platform. The simulated results shown in Fig. 6 are presented in the form of insertion loss and power imbalance as comparisons. The measured insertion loss and power imbalance are both under 1 dB within a 300 nm bandwidth.

A comparison of the performance of several MMIs using different structures and materials is shown in Table 1. Thanks to the SWG structure, the MMI demonstrated in this work shows a much larger 1 dB bandwidth compared to other previously demonstrated MMIs on the Si_3N_4/SiO_2 platform. Also, its performance is comparable to the best devices demonstrated on the SOI platform.

Table 1. Comparison of several experimentally demonstrated MMIs

MMI ref.	1 dB bandwidth	Design	Platform
[39]	1505-1635 nm (130 nm)	Paired / Conventional	Si_3N_4/SiO_2
	1555-1590 nm (35 nm)	General / Conventional	Si_3N_4/SiO_2
[35]	685-745 nm (60 nm)	Paired / Conventional	Si_3N_4/SiO_2
	700-745 nm (45 nm)	General / Conventional	Si_3N_4/SiO_2
[40]	(Insertion loss > 5 dB)	General / Conventional	Si_3N_4/SiO_2
[13]	1400-1700nm (300 nm)	General / SWG	SOI
[41]	1470-1700nm (230 nm)	General / SWG	SOI
[28]	1500-1640 (140 nm)	General / Bricked SWG	SOI
[42]	(2 dB bandwidth 380 nm)	General / SWG	SOI
This work	1375-1675 nm (300 nm)	Paired / SWG	Si_3N_4/SiO_2

Figure 13 shows the measured transmission spectrum of the paired SWG MMI at shorter wavelengths using a tunable laser source working around 1310 nm. As anticipated, we observed a distinct drop in the spectrum around 1260 nm, which can be attributed to the Bragg grating limitation.

Optics EXPRESS

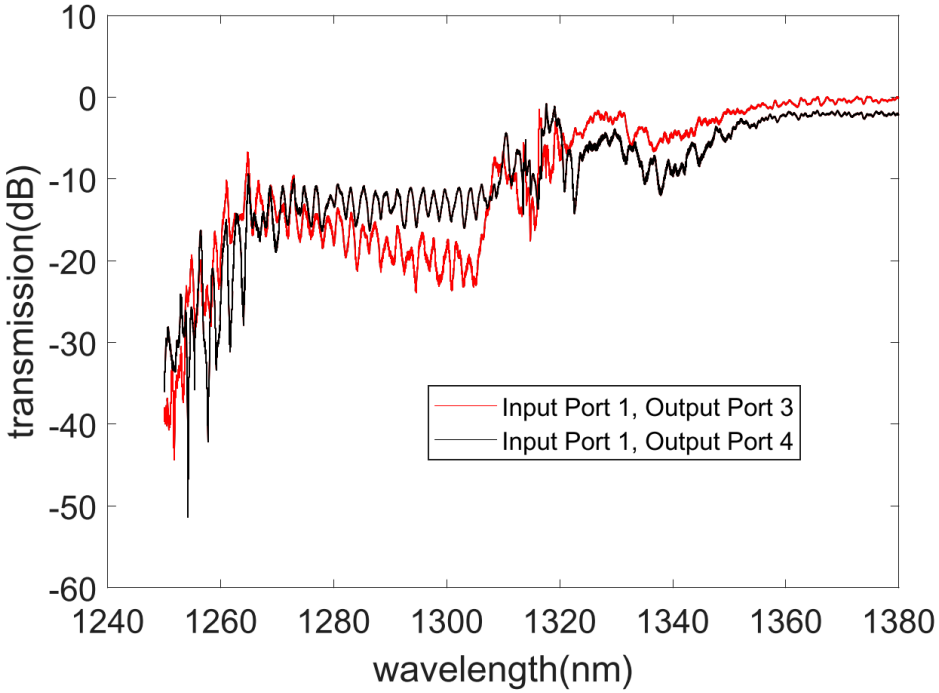

Fig. 13. Measured transmission spectrum of the paired SWGMMI for shorter wavelengths using TSL, normalized to the reference line. The spectrum shows the Bragg grating drop around 1260 nm, as predicted by our simulations shown in Fig. 6.

5. Conclusions

In conclusion, we have generalized the theory of subwavelength grating multimode interference coupler to the silicon nitride platform and have demonstrated an ultra-broadband beam splitter both by simulation and experiment. Specifically, by following a two-step strategy, starting with a non-paired SWG MMI and then progressing to a paired SWG MMI, we have achieved significant improvements in performance compared to conventional MMIs. The paired SWG MMI exhibits a remarkable 1 dB bandwidth of 300 nm, showcasing its potential as a high-performance component for the Si_3N_4/SiO_2 platform. This device can serve as a valuable component in broadband integrated photonic circuits and will have wide applications in coherent astrophotonics, sensing, spectroscopy, and quantum photonics.

Funding. National Science Foundation (ECCS #2219760); NASA Headquarters (21-APRA-21-0116).

Disclosures. The authors declare no conflicts of interest.

Data availability. Data underlying the results presented in this paper are not publicly available at this time but may be obtained from the authors upon reasonable request.

References

1. H. F. Talbot, "LXXVI. Facts relating to optical science. No. IV," The London. Edinburgh, and Dublin Philosophical Magazine and Journal of Science **9**(56), 401–407 (1836).
2. R. Ulrich and G. Ankele, "Self-imaging in homogeneous planar optical waveguides," Appl. Phys. Lett. **27**(6), 337–339 (1975).
3. L. B. Soldano and E. C. Pennings, "Optical multi-mode interference devices based on self-imaging: principles and applications," J. Lightwave Technol. **13**(4), 615–627 (1995).
4. D. W. Kim, A. Barkai, R. Jones, *et al.*, "Silicon-on-insulator eight-channel optical multiplexer based on a cascade of asymmetric Mach–Zehnder interferometers," Opt. Lett. **33**(5), 530–532 (2008).

Optics EXPRESS

5. D. Kwong, Y. Zhang, A. Hosseini, *et al.*, "1 × 12 even fanout using multimode interference optical beam splitter on silicon nanomembrane," Electron. Lett. **46**(18), 1281–1283 (2010).
6. M. Bachmann, P. Besse, and H. Melchior, "Overlapping-image multimode interference couplers with a reduced number of self-images for uniform and nonuniform power splitting," Appl. Opt. **34**(30), 6898–6910 (1995).
7. B. Rahman, N. Somasiri, C. Themistos, *et al.*, "Design of optical polarization splitters in a single-section deeply etched MMI waveguide," Appl. Phys. B **73**(5-6), 613–618 (2001).
8. R. Halir, G. Roelkens, A. Ortega-Moñux, *et al.*, "High-performance 90 hybrid based on a silicon-on-insulator multimode interference coupler," Opt. Lett. **36**(2), 178–180 (2011).
9. A. Ortega-Monux, L. Zavargo-Peche, A. Maese-Novo, *et al.*, "High-performance multimode interference coupler in silicon waveguides with subwavelength structures," IEEE Photon. Technol. Lett. **23**(19), 1406–1408 (2011).
10. D. S. Levy, R. Scarmozzino, and R. M. Osgood, "Length reduction of tapered N x N MMI devices," IEEE Photon. Technol. Lett. **10**(6), 830–832 (1998).
11. I. Molina-Fernandez, A. Ortega-Moñux, and J. G. Wangüemert-Pérez, "Improving multimode interference couplers performance through index profile engineering," J. Lightwave Technol. **27**(10), 1307–1314 (2009).
12. A. Maese-Novo, R. Halir, S. Romero-García, *et al.*, "Wavelength independent multimode interference coupler," Opt. Express **21**(6), 7033–7040 (2013).
13. R. Halir, P. Cheben, J. M. Luque-González, *et al.*, "Ultra-broadband nanophotonic beamsplitter using an anisotropic sub-wavelength metamaterial," Laser Photonics Rev. **10**(6), 1039–1046 (2016).
14. H. Kikuta, Y. Ohira, and K. Iwata, "Achromatic quarter-wave plates using the dispersion of form birefringence," Appl. Opt. **36**(7), 1566–1572 (1997).
15. R. Halir, P. Cheben, J. Schmid, *et al.*, "Continuously apodized fiber-to-chip surface grating coupler with refractive index engineered subwavelength structure," Opt. Lett. **35**(19), 3243–3245 (2010).
16. P. Cheben, D. Xu, S. Janz, *et al.*, "Subwavelength waveguide grating for mode conversion and light coupling in integrated optics," Opt. Express **14**(11), 4695–4702 (2006).
17. P. Cheben, P. J. Bock, J. H. Schmid, *et al.*, "Refractive index engineering with subwavelength gratings for efficient microphotonic couplers and planar waveguide multiplexers," Opt. Lett. **35**(15), 2526–2528 (2010).
18. P. J. Bock, P. Cheben, J. H. Schmid, *et al.*, "Subwavelength grating periodic structures in silicon-on-insulator: a new type of microphotonic waveguide," Opt. Express **18**(19), 20251–20262 (2010).
19. U. Levy, M. Abashin, K. Ikeda, *et al.*, "Inhomogenous dielectric metamaterials with space-variant polarizability," Phys. Rev. Lett. **98**(24), 243901 (2007).
20. P. J. Bock, P. Cheben, J. H. Schmid, *et al.*, "Subwavelength grating crossings for silicon wire waveguides," Opt. Express **18**(15), 16146–16155 (2010).
21. D. González-Andrade, J. G. Wangüemert-Pérez, A. V. Velasco, *et al.*, "Ultra-broadband mode converter and multiplexer based on sub-wavelength structures," IEEE Photonics J. **10**(2), 1–10 (2018).
22. D. González-Andrade, R. F. de Cabo, J. Vilas, *et al.*, "Mode converter and multiplexer with a subwavelength phase shifter for extended broadband operation," IEEE Photon. Technol. Lett. **33**(22), 1262–1265 (2021).
23. D. González-Andrade, J. M. Luque-González, J. G. Wangüemert-Pérez, *et al.*, "Ultra-broadband nanophotonic phase shifter based on subwavelength metamaterial waveguides," Photonics Res. **8**(3), 359–367 (2020).
24. I. Glesk, P. J. Bock, P. Cheben, *et al.*, "All-optical switching using nonlinear subwavelength Mach-Zehnder on silicon," Opt. Express **19**(15), 14031–14039 (2011).
25. L. Liu, Q. Deng, and Z. Zhou, "An ultra-compact wavelength diplexer engineered by subwavelength grating," IEEE Photon. Technol. Lett. **29**(22), 1927–1930 (2017).
26. A. Herrero-Bermello, J. M. Luque-González, A. V. Velasco, *et al.*, "Design of a broadband polarization splitter based on anisotropy-engineered tilted subwavelength gratings," IEEE Photonics J. **11**(3), 1–8 (2019).
27. H. Shiran and O. Liboiron-Ladouceur, "Dual-mode broadband compact 2× 2 optical power splitter using sub-wavelength metamaterial structures," Opt. Express **29**(15), 23864–23876 (2021).
28. J. M. Luque-González, A. Ortega-Moñux, R. Halir, *et al.*, "Bricked subwavelength gratings: a tailorable on-chip metamaterial topology," Laser Photonics Rev. **15**(6), 2000478 (2021).
29. C. Pérez-Armenta, A. Ortega-Moñux, J. M. Luque-González, *et al.*, "Polarization-independent multimode interference coupler with anisotropy-engineered bricked metamaterial," Photonics Res. **10**(4), A57–A65 (2022).
30. Y.-W. Hu, Y. Zhang, P. Gatkine, *et al.*, "Characterization of low loss waveguides using Bragg gratings," IEEE J. Select. Topics Quantum Electron. **24**(4), 1–8 (2018).
31. X. Ji, F. A. Barbosa, S. P. Roberts, *et al.*, "Ultra-low-loss on-chip resonators with sub-milliwatt parametric oscillation threshold," Optica **4**(6), 619–624 (2017).
32. D. J. Blumenthal, R. Heideman, D. Geuzebroek, *et al.*, "Silicon nitride in silicon photonics," Proc. IEEE **106**(12), 2209–2231 (2018).
33. R. Halir, P. J. Bock, P. Cheben, *et al.*, "Waveguide sub-wavelength structures: a review of principles and applications," Laser Photonics Rev. **9**(1), 25–49 (2015).
34. D. B. Leviton and B. J. Frey, "Temperature-dependent absolute refractive index measurements of synthetic fused silica," in *Optomechanical Technologies for Astronomy* (SPIE 2006), pp. 800–810.
35. M. Sanna, A. Baldazzi, G. Piccoli, *et al.*, "SiN integrated photonic components in the Visible to Near-Infrared spectral region," arXiv, arXiv:2311.16016 (2023).

Optics EXPRESS

36. S. Xie, S. Veilleux, and M. Dagenais, "On-chip high extinction ratio single-stage Mach-Zehnder interferometer based on multimode interferometer," IEEE Photonics J. **14**(6), 1–11 (2022).
37. https://www.photond.com.
38. İ. Navruz and A. Altuncu, "Design of a chirped fiber Bragg grating for use in wideband dispersion compensation," in *New Trends In Computer Networks* (World Scientific, 2005), pp. 114–123.
39. S. Xie, J. Zhan, Y. Hu, *et al.*, "Add–drop filter with complex waveguide Bragg grating and multimode interferometer operating on arbitrarily spaced channels," Opt. Lett. **43**(24), 6045–6048 (2018).
40. J. F. Ruedas, J. Sabek, T. D. Bucio, *et al.*, "Basic building blocks development for a SiN platform in the visible range," in *2021 IEEE 17th International Conference on Group IV Photonics (GFP)* (IEEE 2021), pp. 1–2.
41. V. Vakarin, D. Melati, T. T. D. Dinh, *et al.*, "Metamaterial-engineered silicon beam splitter fabricated with deep UV immersion lithography," Nanomaterials **11**(11), 2949 (2021).
42. W. K. K. Kan, S. Toxqui-Rodriguez, D. Medina-Quiroz, *et al.*, "2 × 2 Ultra-Broadband Multimode Interference Coupler with Subwavelength Gratings Fabricated by Immersion Lithography," in *2023 Photonics North (PN)* (IEEE 2023), pp. 1.